



Cite this: *J. Mater. Chem. C*,
2024, 12, 11824

Bifunctional upconverting luminescent-magnetic $\text{FeS}_2@\text{NaYF}_4:\text{Yb}^{3+},\text{Er}^{3+}$ core@shell nanocomposites with tunable luminescence for temperature sensing[†]

Przemysław Woźny, ^{*a} Kevin Soler-Carracedo, ^a Marcin Perzanowski, ^b Jan Moszczyński, ^a Stefan Lis ^a and Marcin Runowski ^{*a}

Advanced optically active materials have experienced significant development in recent years. Light-emitting materials combined with materials that exhibited magnetic properties result in bifunctional materials with an expanded range of capabilities and applications. New functionalities as a result of the core@shell structure enable interactions with the light and the external magnetic field as well. Continuous progress in materials science leads to innovations that enhance data storage and transmission, bioimaging, sensing, optical thermometry, and other applications crucial to advanced technology. In this research, we have focused on the optimization of the synthesis of a nano-sized FeS_2 material as an optically active, magnetic component of the core, and $\text{NaYF}_4:\text{Yb}^{3+},\text{Er}^{3+}$ nanoparticles (NPs) as a temperature sensitive, up-conversion (UC) luminescence part of the shell. The synthesized core@shell type nanocomposite (NC) material $\text{FeS}_2@\text{NaYF}_4:\text{Yb}^{3+},\text{Er}^{3+}$ exhibits simultaneously the unique features of the core and shell components. The recorded UC emission spectra under 975 nm laser excitation show the possibility of tuning the UC luminescence color with the application of a highly absorbing FeS_2 component in the composite material. Moreover, the magnetic properties of the FeS_2 core nanoparticles and the synthesized NC were compared to confirm the potential application of the NC as a novel bifunctional luminescent-magnetic sensing platform. For both materials the luminescence color changed with the increasing laser power density, allowing color-tunable light generation. Additionally, optical temperature sensing properties of the NPs and NC were compared, resulting in a very high relative temperature sensitivity of $\sim 2.0\% \text{ K}^{-1}$ for both materials.

Received 20th March 2024,
Accepted 26th June 2024

DOI: 10.1039/d4tc01117a

rsc.li/materials-c

1. Introduction

Nanoparticles with both magnetic and luminescent properties have emerged as a fascinating area of research with wide-ranging implications in various fields, from medicine to electronics.^{1–3} Multifunctional nanomaterials with combined unique properties *i.e.*, magnetism and luminescence, open up new possibilities for innovative applications. In the realm of electronics and information technology, nanoparticles with magnetic and luminescent properties find applications in data storage and sensing properties.^{4–6} Magnetic nanoparticles are crucial for high-density data storage, offering non-volatile

memory with low energy consumption. The integration with luminescent properties can enable also novel display technologies, quantum dot-based LEDs, and optoelectronic devices.

Iron sulfides are materials composed of Fe and S, some of the most common elements in the lithosphere. Iron sulfides can be present in several types *i.e.*, troilite (FeS), pyrrhotite ($\text{Fe}_{(1-x)}\text{S}$, $x = 0\text{--}0.2$), pyrite (FeS_2), marcasite (FeS_2), or greigite (Fe_3S_4) which exhibit different electronic and optical properties.^{7–9} Pyrite FeS_2 with a cubic crystal structure (known as “fool’s gold”) is composed of some of the most earth-abundant elements *i.e.*, Fe and S elements which determine the low price of such materials. Pyrite FeS_2 was proposed as a semiconducting material for photovoltaic solar cells, energy conversion, energy storage, electrode materials, photocatalysis for reactive oxygen species generation and sensors.^{10–13} The paramagnetic properties of FeS_2 with the pyrite structure due to the reduction of the S^- on the surface of the material were previously reported.^{14,15} Several investigations of iron sulfides *e.g.*, marcasite, reported earlier are based primarily on the

^a Adam Mickiewicz University, Faculty of Chemistry, Uniwersytetu Poznańskiego 8, 61-614 Poznań, Poland. E-mail: przemyslaw.wozny@amu.edu.pl, runowski@amu.edu.pl

^b Institute of Nuclear Physics Polish Academy of Sciences, Radzikowskiego 152, 31-342, Kraków, Poland

† Electronic supplementary information (ESI) available. See DOI: <https://doi.org/10.1039/d4tc01117a>

magnetic and electrical properties.¹ Magnetic properties have indicated a very weak temperature-independent paramagnetism. It is important to obtain a pure phase of iron sulfides without impurities from other phases to provide the desired properties of materials. Many synthesis procedures of pure phase FeS_2 were previously investigated *e.g.*, the hydrothermal method,¹¹ the solvothermal method,¹⁶ metal-organic chemical vapor deposition (MOVCD),¹⁷ sulfurization of iron films,¹⁸ *etc.* Other important advantages of iron sulfides are their light absorption properties and the possibility to be applied as optically active materials. Because of changing the band gap energy (0.96–1.76 eV) in different iron sulfides with miscellaneous size and morphology, it is possible to utilize plasmonic effects occurring in this type of nanocrystal.^{19–21} Nanosized FeS_2 particles present a broad absorption band from the UV to the near infrared (NIR) region of the spectrum.¹⁰ Nanosized FeS_2 is a good candidate for core@shell nanocomposites due to its magnetic and optical activity in a broad range of the electromagnetic spectrum.

The unique upconversion (UC) properties of the NaYF_4 : Yb^{3+} , Er^{3+} crystals are well known.^{22,23} It was chosen as the shell material because of explicit anti-Stokes and upconversion luminescence properties after excitation with a 975 nm laser due to incorporation of Yb^{3+} and Er^{3+} dopant ions. The two photons with low energy (NIR) are absorbed by Yb^{3+} ions; energy is transferred to Er^{3+} ions and causes the emission of one photon with a higher energy (in the Vis spectrum region). NaYF_4 is a chemically and physically stable material with a low phonon energy which causes a low probability of multiphoton quenching of UC *i.e.*, absorption of energy by the crystal lattice.^{24,25} Moreover, the emission spectrum of Er^{3+} ions is thermally dependent. Thermally coupled levels (TCLs) of Er^{3+} ions change the luminescence intensity ratio (LIR) under altered temperature conditions. The UC nanomaterials can be applied as bioimaging agents,²⁶ biolabels,²⁷ in theranostics,²⁸ photodynamic therapy,²⁹ data storage,³⁰ as anticounterfeiting materials³¹ and in optical nanomanometry³² and nanothermometry.³³

Composite nanomaterials made of a relevant, functional core and a chemically stable, luminescent shell are the best candidates for advanced applications. Nanocomposites with core@shell structures are promising materials in medicine, photonics, or analytical applications.^{34–37} Here, three different approaches of the iron sulfide core were investigated for pure pyrite FeS_2 synthesis. Nanosized FeS_2 materials were used for further synthesis of the FeS_2 @ NaYF_4 : Yb^{3+} , Er^{3+} nanocomposite with luminescent-magnetic properties. The luminescence and magnetic properties of the NaYF_4 : Yb^{3+} , Er^{3+} shell material and the FeS_2 @ NaYF_4 : Yb^{3+} , Er^{3+} core@shell material were compared. Temperature-dependent luminescence of both materials was investigated.

2. Experimental

FeS_2 synthesis with different Fe^{2+} : S^{2-} Na_2S ratios

The series of iron sulfide materials were obtained using the hydrothermal method. FeCl_2 (0.05 mol) and Na_2S (0.05 mol)

were dissolved separately in 100 mL of demineralized water to prepare a 0.5 M solution. The appropriate amounts of the FeCl_2 solution for the final product (0.00284 mol) were mixed with the addition of deionized water (for 35 mL of final mixture volume). Next, a solution of Na_2S was added dropwise in the Fe^{2+} to S^{2-} ratio of 1:2–1:8 to obtain a pure FeS_2 structure. The prepared black solutions were transferred to Teflon-lined vessels, and a hydrothermal reaction occurred for 12 h at 200 °C.

FeS_2 synthesis with different surface-active agents

Next, 0.00284 mol surface active agents *e.g.*, poly(acrylic acid) (PAA), polyvinylpyrrolidone (PVP), poly(vinyl alcohol) (PVA), trisodium citrate (Na_3cit), diammonium citrate (NH_4cit), cetyltrimethylammonium bromide (CTAB), and polyethylene glycol (PEG) were mixed with 20 mL of water and the FeCl_2 solution (0.00284 mol). After 30 min, an appropriate volume of Na_2S (1:2 Fe^{2+} : S^{2-} ratio) was added dropwise. As prepared solutions were transferred to Teflon-lined vessels. Iron sulfides were synthesized using the hydrothermal method for 12 h at 200 °C.

Nanocomposite synthesis

The FeS_2 (40 mg) synthesized with PAA was mixed in 20 mL of water in an ultrasound bath to form a stable colloid. Next, the PAA solution (0.67 mL, 0.5 M) was added to the colloidal solution of FeS_2 with mixing. After 10 min, an appropriate volume of 0.5 M LnCl_3 ($\text{Ln} = \text{Y, Yb, Er}$) solutions was added to obtain 0.0013 mol NaYF_4 :20% Yb^{3+} , 2% Er^{3+} . After 30 min, a stoichiometric amount of NaF (0.5 M) was added slowly dropwise with mixing. Emerging turbidity of the solutions was observed. The FeS_2 @ NaYF_4 : Yb^{3+} / Er^{3+} material slowly precipitated as a result of NaYF_4 shell formation on the FeS_2 core. After 1 h, the synthesized nanocomposites (NCs) were centrifuged three times with demineralized water, dried at 80 °C for 20 h and ground. Additionally, pure luminophores *i.e.*, NaYF_4 :20% Yb, 2% Er nanoparticles (NPs) were also obtained with the same methodology without using FeS_2 nanoparticles.

Apparatus

Powder X-ray diffraction (XRD) patterns were recorded using a Bruker AXS D8 Advance diffractometer in the Bragg–Brentano geometry, with $\text{Cu K}\alpha 1$ radiation ($\lambda = 1.5406 \text{ \AA}$) and 0.05° step scan mode. The reference data were taken from the ICSD (Inorganic Crystal Structure Database). Absorption spectra were recorded using a JASCO V-770 spectrophotometer, equipped with a spherical integrator ILN-925 with two detectors, *i.e.*, a photomultiplier in the UV-Vis range ($\lambda = 200$ –850 nm) and a Pbs detector in the NIR range ($\lambda = 850$ –1600 nm), and two radiation sources, *i.e.*, the deuterium ($\lambda = 190$ –340 nm) and the halogen lamps ($\lambda = 340$ –1600 nm). Transmission electron microscopy (TEM) images were taken with a Hitachi HT7700 microscope, applying an acceleration voltage of 100 kV. Energy-dispersive X-ray (EDX) analysis with elemental mapping was done with a scanning electron microscope FEI Quanta 250 FEG equipped with an EDAX detector. Dynamic light scattering (DLS) and zeta potential measurements were performed using a Malvern Zetasizer Nano ZS. The luminescence properties of the materials,



i.e., emission spectra at room, low and high temperature, were investigated using an Andor Shamrock 500i spectrometer with a silicon CCD iDus camera as the detector. Materials were excited using a fiber-coupled solid-state CNI laser FC-975-2W. The quantum yield was measured using an integrating sphere. The measurements were corrected for the apparatus response. The varied temperature conditions with 0.1 °C set point resolution were generated with the THMS 600 heating–cooling stage from Linkam. Magnetic properties were investigated at temperatures ranging from 5 K to 300 K with a Quantum Design MPMS SQUID magnetometer.

3. Results and discussion

Structural analysis

Fig. 1 presents the XRD patterns of the iron sulfide materials synthesized with the use of varied Fe²⁺ to S²⁻ ion ratios (Fe:S) used in synthesis (a), materials obtained in the presence of different additives worked as surface-active agents (b) and as the synthesized crystal structures of the NaYF₄:Yb³⁺,Er³⁺ luminescent core and FeS₂@NaYF₄:Yb³⁺,Er³⁺ core@shell material. The materials with different F:S ratios used in the synthesis show an altered crystal structure (Fig. 1a). The smallest amount of S²⁻ ions (1:2 Fe:S) in the synthesis results in a crystalline cubic FeS₂ pyrite structure from the *Pa-3* space group. An increased Fe:S ratio (from 1:3–1:5) results in crystallization of an additional, orthorhombic marcasite phase from the *Pnmm* space group. Additional reflexes of cubic magnetite (Fe₂O₃) from the *Fd*³ space group can also be seen in materials with 1:4 and 1:5 Fe:S ratios, which is obtained as a result of

alkaline pH from the excess of added Na₂S solution. A further increase of Na₂S amount causes the formation of the amorphous tetragonal mackinawite from the *P₄nmm* space group. Narrow reflexes of pyrite were evidence of the micrometric size of obtained crystals.³⁸ The next step was the investigation of the synthesis process of the pyrite nanocrystals using a fixed Fe:S ratio and different surface active agents (Fig. 1b). Only the use of PVA, PAA, and CTAB results in the crystallization of the pure FeS₂ pyrite structure with different micrometric (PVA) and nanometric sizes (CTAB and PAA). Based on the PAA-assisted FeS₂ synthesis, a suitable protocol of the NaYF₄, the FeS₂@NaYF₄:Yb³⁺,Er³⁺ composite material was obtained. NaYF₄:Yb³⁺,Er³⁺ crystallizes in the cubic structure from the *Fm*³*m* space group. The same main phase was observed in the NC structure, but here, minor reflexes from cubic FeS₂ as evidence of the successful core@shell structure formation were also observed (Fig. 1c).

The Raman spectra of the FeS₂ NPs and FeS₂@NaYF₄:Yb³⁺,Er³⁺ NC are presented in Fig. 1d. The spectra of the pure FeS₂ core show characteristic A_g and E_g phonon modes of FeS₂ at 336 cm⁻¹ and 380 cm⁻¹, respectively. Additional low intensity T_g modes at 358 cm⁻¹ and 420 cm⁻¹ were also visible. The recorded spectra and values of the phonon modes obtained agree with the literature data and confirm the synthesis of pure FeS₂ and its presence in the synthesized nanocomposites.³⁹ The broadened peaks (phonon modes) of the recorded Raman spectra are due to the small crystal size of the FeS₂ nanoparticles.⁷ The observed broad vibrational modes in the ranges of 150–300 cm⁻¹ (vibrational modes of Y–F in the lattice) and 550–1000 cm⁻¹ (vibrational modes of Na–F in the lattice) are the evidence of the presence of the NaYF₄ cubic structure in

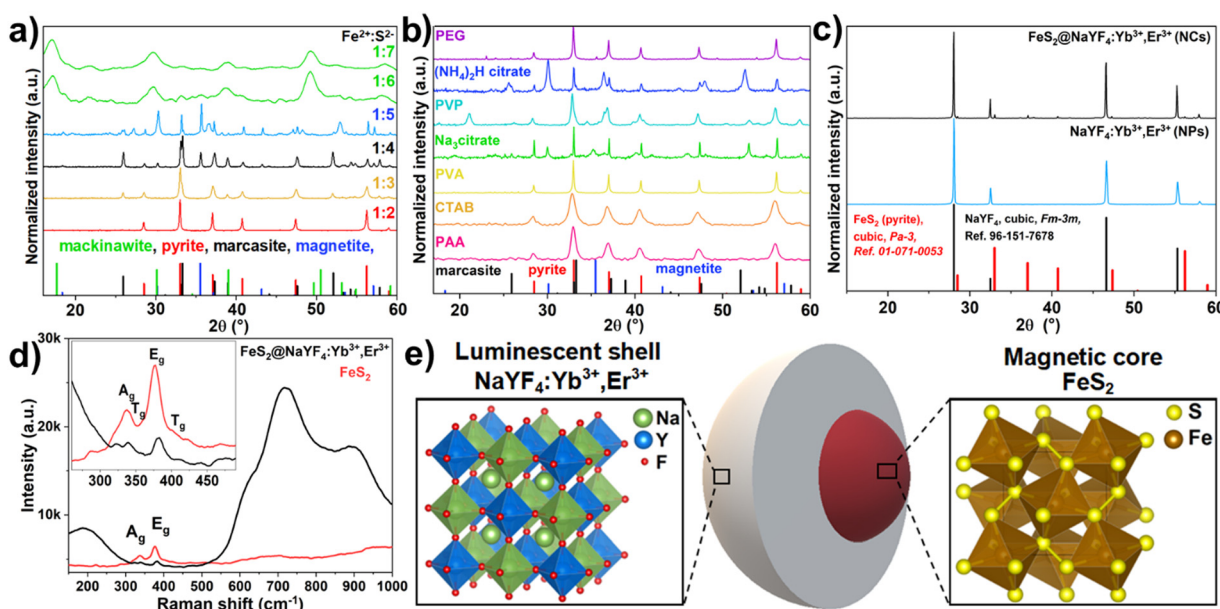


Fig. 1 Powder XRD patterns of the FeS₂ materials obtained with altered Fe:S ratio (a), obtained in the presence of additives in the synthesis process (b) as well as for the pure NaYF₄:Yb₃₊,Er³⁺ NPs and FeS₂@NaYF₄:Yb³⁺,Er³⁺ NC (c), Raman spectra of the FeS₂ NPs and FeS₂@NaYF₄:Yb³⁺,Er³⁺ NC indicating phonon modes of the FeS₂ in the synthesized materials (d), and scheme of the core@shell composition and visualization of the crystal structure of the core and shell components (e).



the resulting NC material.^{40–42} In the inset in Fig. 1d, a magnification of the spectrum range with the characteristic FeS_2 modes is presented, to show the presence of FeS_2 in the NC. In Fig. 1e the scheme of the composition of the as-prepared $\text{FeS}_2@\text{NaYF}_4:\text{Yb}^{3+},\text{Er}^{3+}$ NC, *i.e.*, core@shell material is presented. Additionally, visualization of the crystal structure of the cubic NaYF_4 and cubic FeS_2 materials is presented (Fig. 1e).

Morphology of nanocomposites

The transmission electron microscopy (TEM) images of the obtained FeS_2 NPs and the $\text{FeS}_2@\text{NaYF}_4:\text{Yb}^{3+},\text{Er}^{3+}$ NC are presented in Fig. 2a and b, respectively. The obtained FeS_2 NPs have a low size distribution, *i.e.*, 4 ± 1 nm (inset in Fig. 2a); however, they are significantly aggregated. The TEM image of the synthesized NC present dense particles of the material with broad size distribution composed of smaller, aggregated particles (Fig. 2b). The mean size of the NC particles was estimated as 319 ± 84 nm (inset in Fig. 2b). Additionally, the size of the FeS_2 core and $\text{FeS}_2@\text{NaYF}_4:\text{Yb}^{3+},\text{Er}^{3+}$ core@shell materials were compared using DLS (see. Fig. S1a, ESI[†]). The measured zeta potential for the NCs was 21.52 ± 3.21 mV which may indicate the tendency of particles to agglomerate. Although the particle size is too large for biological applications, it still

holds potential for use in *e.g.*, photonics, electronics, memories, sensing, or modern catalysis. Fig. 2c–h presents elemental mapping images of the $\text{FeS}_2@\text{NaYF}_4:\text{Yb}^{3+},\text{Er}^{3+}$ NC material. Elements of the $\text{NaYF}_4:\text{Yb}^{3+},\text{Er}^{3+}$ shell material *i.e.*, Na, Y, F and Er (Fig. S1b, ESI[†]) are equally distributed in the material and the S and Fe elements are grouped in specific regions of material. These results indicate the coexistence of these elements in the final nanocomposite product. Moreover, the EDX spectrum shows the presence of all mentioned elements in the synthesized nanocomposite material (Fig. S1c, ESI[†]).

The absorption spectra for the FeS_2 NPs, $\text{NaYF}_4:\text{Yb}^{3+},\text{Er}^{3+}$ NPs, and $\text{FeS}_2@\text{NaYF}_4:\text{Yb}^{3+},\text{Er}^{3+}$ NC were recorded from 200 to 1600 nm and are presented in Fig. 3a. The synthesized FeS_2 NPs show a broad absorption band from UV to NIR region, with the maximum at $\lambda = 250$ nm (top). Absorption intensity decreases gradually and reaches the minimum at $\lambda \approx 1350$ nm. Moreover, a weak absorption band is observed at $\lambda \approx 600$ nm, due to the weak plasmonic properties of the FeS_2 material.²¹ The absorption spectrum for the $\text{NaYF}_4:\text{Yb}^{3+},\text{Er}^{3+}$ NPs (center) clearly shows numerous, characteristic 4f–4f absorption bands of the Er^{3+} ions, *e.g.*, at 276 nm ($^4\text{I}_{15/2} \rightarrow ^4\text{G}_{7/2}$ transition), 520 nm ($^4\text{I}_{15/2} \rightarrow ^4\text{H}_{11/2}$), 652 nm ($^4\text{I}_{15/2} \rightarrow ^4\text{F}_{9/2}$) and 978 nm ($^4\text{I}_{15/2} \rightarrow ^4\text{I}_{11/2}$), which overlap with the Yb^{3+} absorption band at

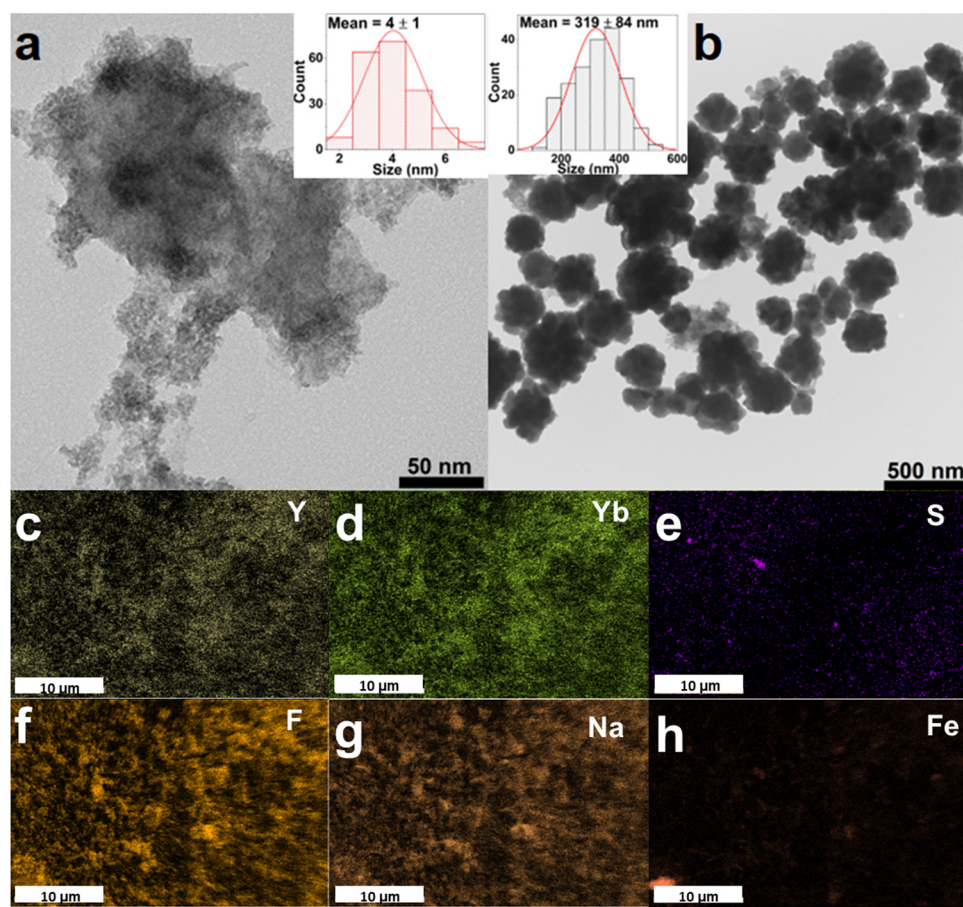


Fig. 2 The representative TEM images of the FeS_2 NPs (a) and $\text{FeS}_2@\text{NaYF}_4:\text{Yb}^{3+},\text{Er}^{3+}$ NC (b); the insets show histograms of the NPs and NC size distribution. The EDX mapping of elements in the $\text{FeS}_2@\text{NaYF}_4:\text{Yb}^{3+},\text{Er}^{3+}$ NC, *i.e.*, Y (c), Yb (d), S (e), F (f), Na (g), Fe (h).



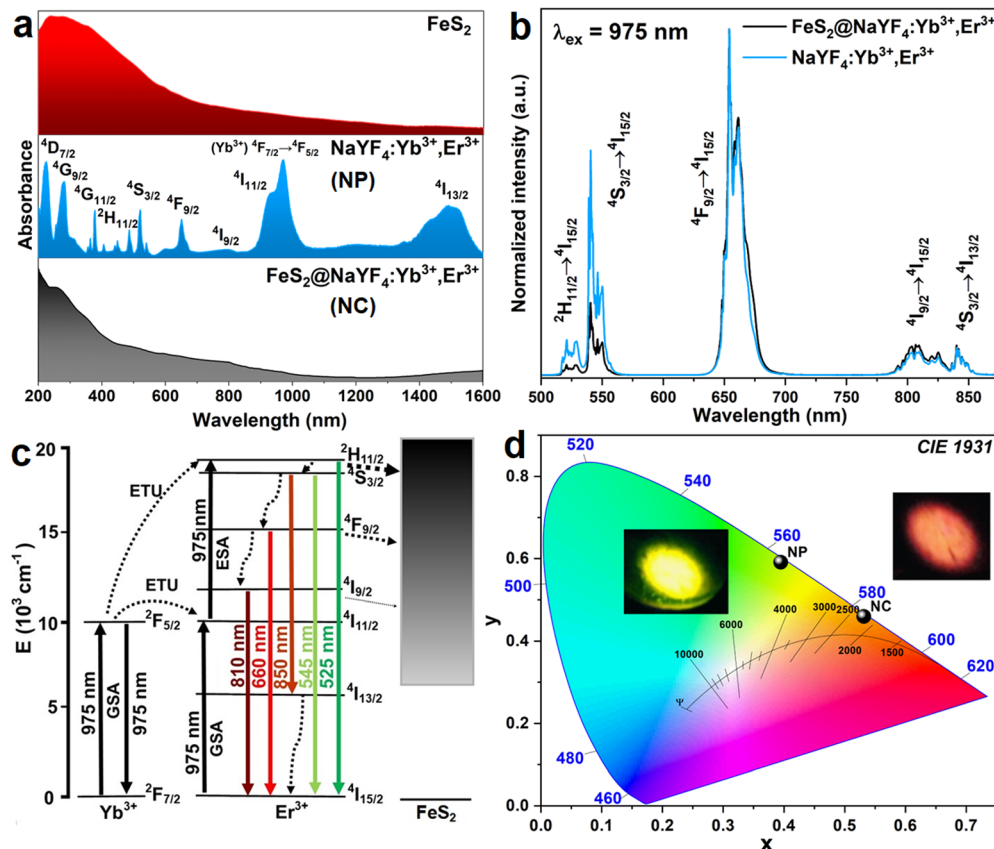


Fig. 3 Absorption spectra of the FeS_2 NPs (red), $\text{NaYF}_4:\text{Yb}^{3+},\text{Er}^{3+}$ NPs (blue), and $\text{FeS}_2@\text{NaYF}_4:\text{Yb}^{3+},\text{Er}^{3+}$ NC (black) (a). Normalized UC luminescence emission spectra of the $\text{NaYF}_4:\text{Yb}^{3+},\text{Er}^{3+}$ NPs (blue), and the $\text{FeS}_2@\text{NaYF}_4:\text{Yb}^{3+},\text{Er}^{3+}$ NC (black) under 975 nm laser excitation (b); energy level scheme of UC luminescence for the $\text{FeS}_2@\text{NaYF}_4:\text{Yb}^{3+},\text{Er}^{3+}$ material (c); CIE diagram of the $\text{NaYF}_4:\text{Yb}^{3+},\text{Er}^{3+}$ NPs and $\text{FeS}_2@\text{NaYF}_4:\text{Yb}^{3+},\text{Er}^{3+}$ NC luminescence (d); insets show the visible luminescence of the $\text{NaYF}_4:\text{Yb}^{3+},\text{Er}^{3+}$ NPs (yellowish-green) and $\text{FeS}_2@\text{NaYF}_4:\text{Yb}^{3+},\text{Er}^{3+}$ NC (orange) taken with a digital camera upon laser excitation.

≈ 980 nm ($^4\text{F}_{7/2} \rightarrow ^4\text{F}_{5/2}$).⁴³ Whereas, the absorption spectrum of the synthesized $\text{FeS}_2@\text{NaYF}_4:\text{Yb}^{3+},\text{Er}^{3+}$ NC (bottom) is comparable to bare, highly absorbing FeS_2 NPs, but the influence of the luminescent $\text{NaYF}_4:\text{Yb}^{3+},\text{Er}^{3+}$ shell is visible. Influence of the Ln^{3+} absorption band is particularly seen at $\approx 270, 360, 520, 650, 800, 1000$, and above 1400 nm, which corresponds to Er^{3+} , and Yb^{3+} absorption bands, and it confirms the optical activity of the obtained NC in those ranges.

Upconversion luminescence properties

We have combined the UC luminescence of the $\text{Yb}^{3+}/\text{Er}^{3+}$ -doped NPs with the magnetic properties of the FeS_2 core, mainly due to the large absorption cross section in the NIR (980 nm) of the UC NPs, guaranteeing efficient UC emission, as well as relatively low absorption of the magnetic core in the NIR range. UC emission spectra for the $\text{NaYF}_4:\text{Yb}^{3+},\text{Er}^{3+}$ NPs and the $\text{FeS}_2@\text{NaYF}_4:\text{Yb}^{3+},\text{Er}^{3+}$ NC were investigated using excitation at $\lambda = 975$ nm. Both materials show UC luminescence properties with characteristic emission bands of the Er^{3+} ions, as presented in Fig. 3b. The UC mechanism of the $\text{NaYF}_4:\text{Yb}^{3+},\text{Er}^{3+}$ encompasses absorption of the NIR photon by Yb^{3+} ions in the ground state absorption (GSA) process. Next, energy is transferred to the $^4\text{I}_{11/2}$ excited state of the Er^{3+} ions in the energy

transfer upconversion (ETU) process upon simultaneous relaxation of the Yb^{3+} ions from $^2\text{F}_{5/2}$ excited state to the $^2\text{F}_{7/2}$ ground state (Fig. 3c). Subsequently, the higher energy level *i.e.*, $^2\text{H}_{11/2}$ is populated by second ETU process with the absorption of a second photon with $\lambda = 975$ nm by Yb^{3+} ions and simultaneous non-radiative relaxation of the Yb^{3+} ion. After two ETU processes the visible green emission at $\lambda_{\text{em}} \approx 520$ nm can be observed due to $^2\text{H}_{11/2} \rightarrow ^4\text{I}_{15/2}$ radiative transition. Lower energy levels *i.e.*, $^4\text{S}_{3/2}$, $^4\text{F}_{9/2}$ and $^4\text{I}_{9/2}$ are populated by non-radiative relaxation processes, and then, the emission of radiative transitions $^4\text{S}_{3/2} \rightarrow ^4\text{I}_{15/2}$ ($\lambda_{\text{em}} \approx 550$ nm), $^4\text{F}_{9/2} \rightarrow ^4\text{I}_{15/2}$ ($\lambda_{\text{em}} \approx 660$ nm), $^4\text{I}_{9/2} \rightarrow ^4\text{I}_{15/2}$ ($\lambda_{\text{em}} \approx 810$ nm) and $^4\text{S}_{3/2} \rightarrow ^4\text{I}_{13/2}$ ($\lambda_{\text{em}} \approx 850$ nm) are observed. Normalized emission spectra show altered intensities of emission bands for the NPs and NC, *i.e.*, a decrease in the emission intensity of the $^4\text{S}_{3/2} \rightarrow ^4\text{I}_{15/2}$ and $^2\text{H}_{11/2} \rightarrow ^4\text{I}_{15/2}$ transitions. Differences in the luminescence intensity ratio (LIR) of the emission bands especially at $\lambda \approx 520$ and 550 nm are evidence of strong reabsorption of the emission in the green region of the spectrum by the FeS_2 core, in the case of the $\text{FeS}_2@\text{NaYF}_4:\text{Yb}^{3+},\text{Er}^{3+}$ NC materials. Comparison of the luminescence intensity is presented in Fig. S2 (ESI†).

For a visual representation of the modified luminescence properties *i.e.*, color-tunable upconversion emission of the



synthesized the $\text{NaYF}_4:\text{Yb}^{3+},\text{Er}^{3+}$ NPs, and the $\text{FeS}_2@\text{NaYF}_4:\text{Yb}^{3+},\text{Er}^{3+}$ NC excited with 975 nm laser, the chromaticity diagram (CIE 1931) with determined color coordinates is presented in Fig. 3d. Based on the recorded emission spectra the coordinates on CIE were calculated as $x_s = 0.395$ and $y_s = 0.591$ for the NPs, and $x_s = 0.531$ and $y_s = 0.460$ for the NC. The presented colors in this CIE diagram agree with the digital photographs of the generated luminescence upon NIR laser irradiation (Fig. 3d). The color purity (CP) parameter represents the percent to which a color resembles its pure color and it is the one of factors for evaluating the utility of luminesophores as a light source. It can be calculated using the below eqn (1):

$$\text{Color purity} = \frac{\sqrt{(x_s - x_i)^2 + (y_s - y_i)^2}}{\sqrt{(x_d - x_i)^2 + (y_d - y_i)^2}} \times 100\% \quad (1)$$

where (x_s, y_s) are calculated material's color coordinates, (x_i, y_i) coordinates for luminescence of the white standard (0.3101, 0.3162), and (x_d, y_d) coordinates at the edge of the CIE diagram on the strait line from (x_i, y_i) , through (x_s, y_s) to the edge of CIE. The CP parameters have been calculated as $\sim 100\%$ for the $\text{NaYF}_4:\text{Yb}^{3+},\text{Er}^{3+}$ NPs, and $\sim 92\%$ for the $\text{FeS}_2@\text{NaYF}_4:\text{Yb}^{3+},\text{Er}^{3+}$ NC UC emission spectra recorded after excited at $\lambda = 975$ nm. High values of the CP parameter are the evidence of the deep luminescence color of as obtained materials. Such high values of the CP parameter are an advantage in the potential use of obtained materials in applications requiring pure emission color, *e.g.*, new light sources. The approach of the utilization of composite materials presents the potential to obtain color-tunable luminescence without a drastic decrease in color purity.

The second important parameter of luminescent materials is correlated color temperature (CCT) which refers to the temperature of black body radiation. The CCT parameter can be calculated using eqn (2):

$$\text{CCT} = -449n^3 + 3525n^2 - 6823n + 5520.33 \quad (2)$$

where n is equal to $(x - 0.332)/(y - 0.186)$ for the CIE 1931. The luminescence of the $\text{NaYF}_4:\text{Yb}^{3+},\text{Er}^{3+}$ NPs has a higher CCT equal to 4543 K, but the $\text{FeS}_2@\text{NaYF}_4:\text{Yb}^{3+},\text{Er}^{3+}$ NC exhibits a lower color temperature of 2265 K.

The next parameter to quantitatively compare the UC luminescence properties is quantum yields (Φ), and it provides information about the conversion efficiency of excitation radiation to emission. Here, the integrated emission spectra for investigated materials (E_s), reflected laser beam form samples (L_s), and from reference material ($L_{\text{La}_2\text{O}_3}$) were analyzed to calculate Φ parameter according to eqn (3):

$$\Phi = \frac{E_s}{L_{\text{La}_2\text{O}_3} - L_s} \times 100\% \quad (3)$$

The Φ value was calculated as 0.0139% for the $\text{NaYF}_4:\text{Yb}^{3+},\text{Er}^{3+}$ NPs, and 0.0015% for the $\text{FeS}_2@\text{NaYF}_4:\text{Yb}^{3+},\text{Er}^{3+}$ NC. Almost 10-times decrease in emission quantum yield is caused by the

strong reabsorption of emitted visible radiation by the FeS_2 core in the core@shell material (see Fig. 3a). It is worth noting that the obtained low values of Φ are typical for UC emission of NPs, which typically are in the range from 0.001 to 0.1%.⁴⁴

The observed, bright UC luminescence encourages us to further analyze the UC luminescence properties of the synthesized nanomaterials. The UC emission spectra of the $\text{NaYF}_4:\text{Yb}^{3+},\text{Er}^{3+}$ NPs and $\text{FeS}_2@\text{NaYF}_4:\text{Yb}^{3+},\text{Er}^{3+}$ NC were recorded as a function of laser power density and presented in Fig. S3a and b (ESI†) respectively. The intensity of emission spectra increases exponentially for both investigated materials under increased pump power density in the experiment, as expected for the non-linear UC processes. Some differences in the emission bands at 550 nm ($^4\text{S}_{3/2} \rightarrow ^4\text{I}_{15/2}$ transition) and 650 nm ($^4\text{F}_{9/2} \rightarrow ^4\text{I}_{11/2}$) can be seen between the $\text{NaYF}_4:\text{Yb}^{3+},\text{Er}^{3+}$ NPs and $\text{FeS}_2@\text{NaYF}_4:\text{Yb}^{3+},\text{Er}^{3+}$ NC. The dependencies of the integrated luminescence intensities (area under the curves) on the varying laser power densities were calculated (Fig. 4a and c). Based on the log-log plot, the n value *i.e.*, the number of photons taking part in the UC processes were calculated using eqn (4):

$$I_{\text{UC}} \propto (I_p)^n \quad (4)$$

where I_{UC} is the integrated intensity, I_p is the calculated laser power density (beam laser power on the given target area), and n is the number of photons involved in the UC mechanism.⁴⁵ The calculated number of photons for both investigated materials are almost identical for bands around $\lambda \approx 550$ nm, 650 nm, and 850 nm with values 2.16, ~ 1.77 , and 2.05, respectively. Only the number of photons for the emission bands at 520 nm ($^2\text{H}_{11/2} \rightarrow ^4\text{I}_{15/2}$ transition) slightly increased from 2.16 to 2.22 ($\Delta n \approx 0.06$), and for emission bands at 800 nm ($^4\text{I}_{9/2} \rightarrow ^4\text{I}_{15/2}$ transition) decreased from 1.71 to 1.66 ($\Delta n \approx 0.05$) after the combination of the luminescent $\text{NaYF}_4:\text{Yb}^{3+},\text{Er}^{3+}$ shell with the FeS_2 core, as a result of emission reabsorption by the FeS_2 core. The values of the n parameter deviate from theoretical values due to cross-relaxation processes induced by the excitation beam.^{46,47} In Fig. 4b and d the CIE diagrams for the emission spectra recorded for increased laser power density are presented. As the laser power increases, we observe a gradual change in the luminescence color from the area of CIE corresponding to the yellow-orange color to the area corresponding to the green color for the $\text{NaYF}_4:\text{Yb}^{3+},\text{Er}^{3+}$ NPs (Fig. 4b). For the $\text{FeS}_2@\text{NaYF}_4:\text{Yb}^{3+},\text{Er}^{3+}$ NC gradual change of the luminescence color from red to orange region was also observed (Fig. 4d). The results are the evidence that there is no significant changes in the upconversion mechanisms in the $\text{NaYF}_4:\text{Yb}^{3+},\text{Er}^{3+}$ NPs and $\text{FeS}_2@\text{NaYF}_4:\text{Yb}^{3+},\text{Er}^{3+}$ NC. Luminescence color change is an effect of the probability of an excited level population of Er^{3+} due to the UC mechanism. In the range of the laser power density used there is no saturation of the excited levels, which is why we can observe changes in the luminescence color. This effect can be applied to the use of developed materials as novel, optical (visual) laser power density sensors based on UC emission color change.⁴⁸



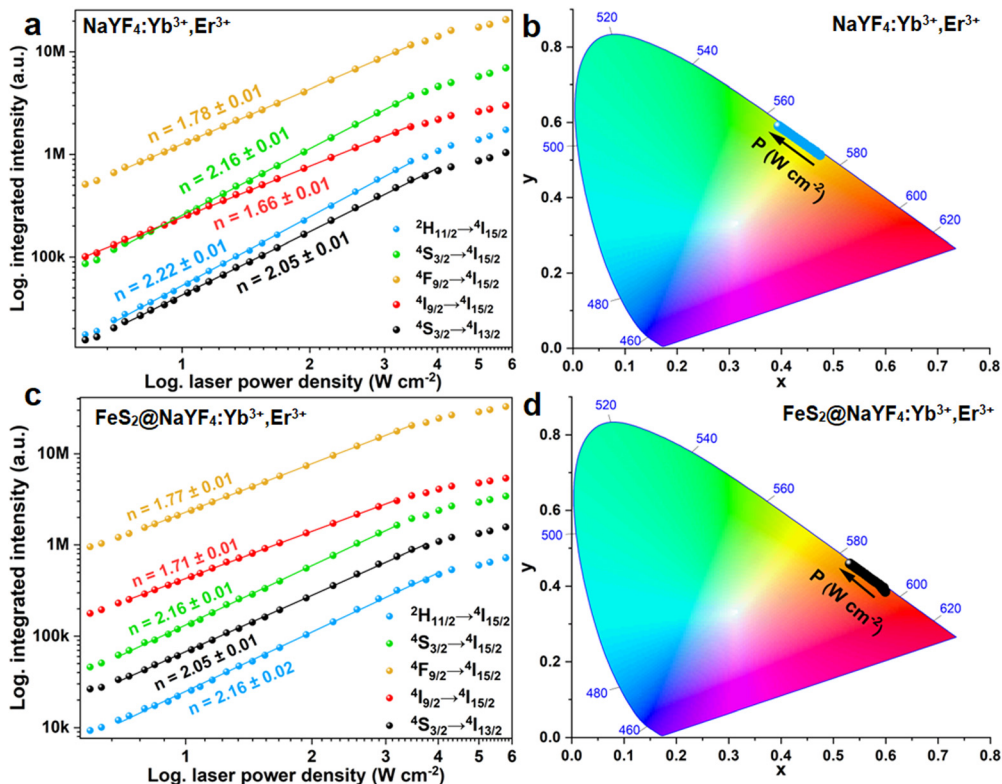


Fig. 4 Integrated luminescence intensity as a function of laser power density for the NaYF₄:Yb³⁺,Er³⁺ NPs (a) and FeS₂@NaYF₄:Yb³⁺,Er³⁺ NC (c). CIE diagrams for the NPs (b) and NC (d) showing the color coordinates as a function of laser power density.

Temperature sensing

The emission intensity of the Er³⁺ ions is thermally dependent, especially the luminescence intensity ratio of TCLs ($\lambda = 520$ nm and $\lambda = 550$ nm) change as a function of temperature.⁴⁹ Here, we compared the UC emission spectra of the NaYF₄:Yb³⁺,Er³⁺ NPs, and the FeS₂@NaYF₄:Yb³⁺,Er³⁺ NC measured at different temperature values (from 200 to 580 K). The luminescence intensity decreases with increasing temperature in the system, due to thermal quenching, *i.e.*, enhanced multi-phonon and cross-relaxation processes (Fig. 5a and d). However, the intensity of different emission bands does not change equally, as it is presented in Fig. 5b and e. The LIR values associated with emissions from TCLs, based on integrated intensities of thermalized Er³⁺ excited levels, were calculated and fitted to the Boltzmann law according to eqn (5):

$$LIR = \frac{I_1}{I_2} = B \exp\left(\frac{\Delta E_{21}}{k_B T}\right) \quad (5)$$

where I_1 is the intensity of the $^2H_{11/2} \rightarrow ^4I_{15/2}$ transition ($\lambda = 520$ nm), I_2 is the intensity of the $^4S_{3/2} \rightarrow ^4I_{15/2}$ transition ($\lambda = 550$ nm), ΔE_{21} is the energy gap between the 520 and 550 nm emission bands, B is a constant, which depends on the spontaneous emission rates, k_B is the Boltzmann constant, and T is the absolute temperature. The LIR parameter shows an almost linear change from 0.15 to 1.25 for the bare NPs and to 1.15 for NC. Next, the relative sensitivities (S_r) were determined for both materials to compare the overall performance of the

investigated materials as optical temperature sensors using eqn (6):

$$S_r = \frac{1}{LIR} \frac{\partial LIR}{\partial T} \times 100\% \quad (6)$$

The S_r parameter as a function of temperature decreases from ~ 2.02 to ~ 0.25 with temperature elevation for both materials, *i.e.*, NaYF₄:Yb³⁺,Er³⁺ and FeS₂@NaYF₄:Yb³⁺,Er³⁺. Next, to determine the accuracy of the temperature sensing we used previously calculated parameters LIR and S_r to determine the temperature resolution parameter according to eqn (7):

$$\delta T = \frac{1}{S_r} \times \frac{\delta LIR}{LIR} \quad (7)$$

where δLIR is the uncertainty of determination of the LIR parameter, related to the signal-to-noise ratio. Here we observed deterioration of the temperature resolution as a function of temperature, namely, from around ≈ 0.1 K at 200 K for both materials to ≈ 0.75 K for NPs and to ≈ 1.00 K for the NC. The bare NaYF₄, Yb³⁺,Er³⁺ shell material shows only slightly better, almost negligible, optical temperature sensing performance. The results confirm the possibility of using a novel, bifunctional luminescent-magnetic FeS₂@NaYF₄:Yb³⁺,Er³⁺ nanocomposite material as well as a popular NaYF₄, Yb³⁺,Er³⁺ upconverting luminophore.



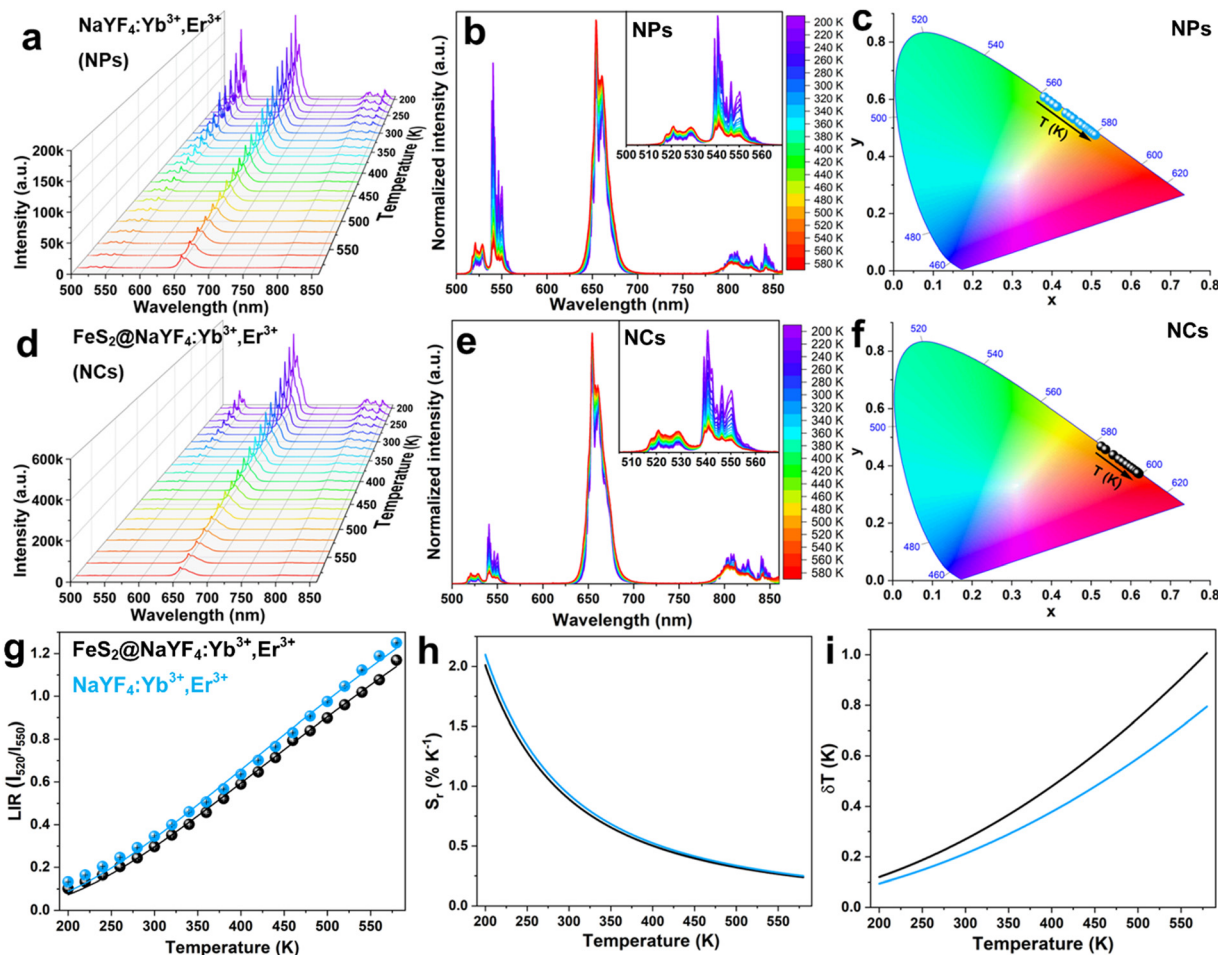


Fig. 5 Non-normalized UC emission spectra of the $\text{NaYF}_4:\text{Yb}^{3+},\text{Er}^{3+}$ NPs (a) and $\text{FeS}_2@\text{NaYF}_4:\text{Yb}^{3+},\text{Er}^{3+}$ NC (d). Normalized UC emission spectra for the $\text{NaYF}_4:\text{Yb}^{3+},\text{Er}^{3+}$ NPs (b) and $\text{FeS}_2@\text{NaYF}_4:\text{Yb}^{3+},\text{Er}^{3+}$ NCs (e); the insets show the magnified region for the bands at $\lambda \approx 525$ and 550 nm (TCLs). Chromaticity coordinates shown in the CIE diagrams for the $\text{NaYF}_4:\text{Yb}^{3+},\text{Er}^{3+}$ NPs (c) and $\text{FeS}_2@\text{NaYF}_4:\text{Yb}^{3+},\text{Er}^{3+}$ NCs (f) as a function of temperature. Calculated LIR (g), relative sensitivity (h), and temperature resolution (i) as a function of temperature for the $\text{NaYF}_4:\text{Yb}^{3+},\text{Er}^{3+}$ NPs (blue) and $\text{FeS}_2@\text{NaYF}_4:\text{Yb}^{3+},\text{Er}^{3+}$ NC (black).

Moreover, we noticed that the luminescence color changed under varying temperature conditions for both materials. Based on the UC emission spectra recorded at different temperatures we calculated the CIE color coordinates x and y for both materials. For the NPs the color changes from green to orange, while for the NC it changes from orange to red with an increase in the temperature of the system. The shift of the chromaticity coordinates as a function of temperature is evidence of the temperature-dependent luminescence color and temperature-driven changes in the UC mechanism for both materials.

Magnetic properties

Zero-field-cooled and field-cooled (ZFC-FC) measurements for both investigated materials were carried out in the external magnetic field of 50 Oe in the temperature range from 5 K to 300 K for both investigated materials. For the FeS_2 NPs, the ZFC-FC curves (Fig. 6a) overlap above the irreversibility temperature (T_{irr}) equal to 280 K. Slightly below the irreversible temperature, at approximately 260 K, is the blocking

temperature (T_b). The presence of both of these temperatures suggests that the FeS_2 NPs undergo a transition between thermally blocked and unblocked states with T_b being an average temperature for the nanoparticles to switch. Above T_{irr} the thermal fluctuation energy overcomes the magnetic anisotropy energy of the particles and the system acts as a paramagnet. Below T_{irr} the anisotropy energy dominates over the thermal energy and the material demonstrates ferromagnetic properties. At low temperature, in both ZFC and FC curves, there is a slight increase of the magnetization which is related to the weak paramagnetic contribution present in the sample. Magnetic hysteresis loops obtained for this sample, measured at different temperatures, are presented in Fig. 6d. The shape of the loops is typical for powdered samples without the preferred easy axis of magnetization. The saturation magnetization decreases monotonously with increasing temperature from 4.5 emu g^{-1} at 5 K to 0.5 emu g^{-1} at 300 K. At 5 K the material reveals clear ferromagnetic behaviors with coercivity of 500 Oe. With rising temperature, coercivity diminishes and at



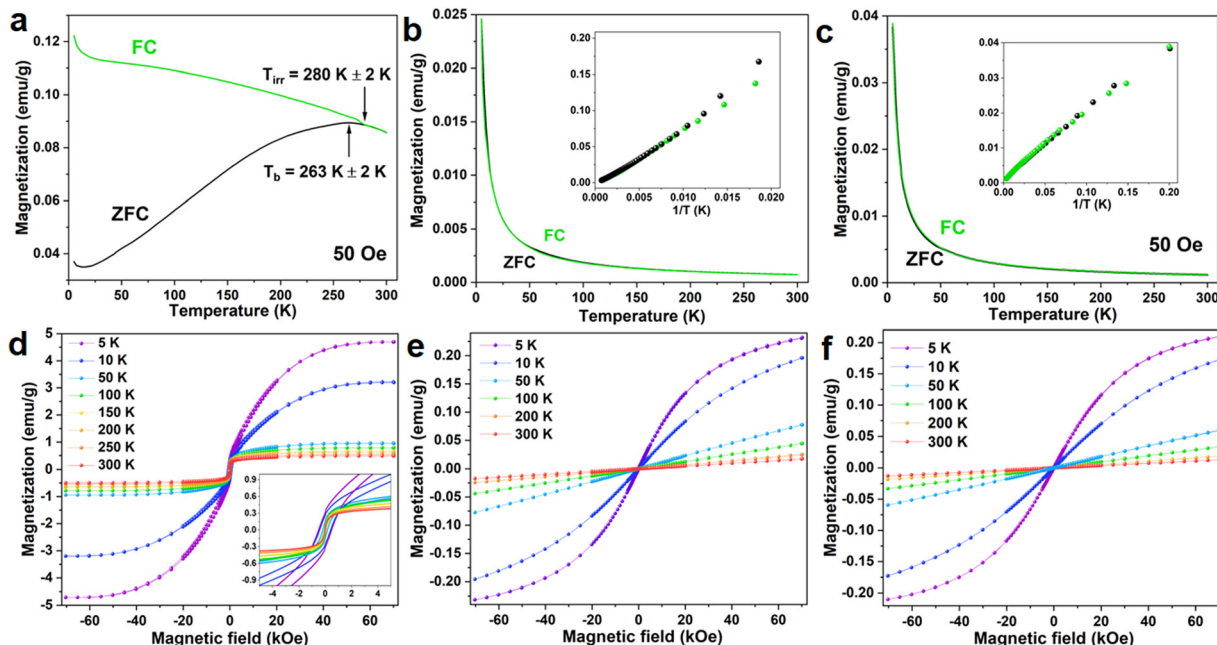


Fig. 6 ZFC-FC curves of the FeS_2 core (a), the $\text{NaYF}_4:\text{Yb}^{3+},\text{Er}^{3+}$ NPs (b) and $\text{FeS}_2@\text{NaYF}_4:\text{Yb}^{3+},\text{Er}^{3+}$ NC (c). Magnetic-field dependence of magnetization at temperatures: 5 K, 10 K, 50 K, 100 K, 200 K, 250 K, and 300 K for the FeS_2 core (d), the $\text{NaYF}_4:\text{Yb}^{3+},\text{Er}^{3+}$ NPs (e) and $\text{FeS}_2@\text{NaYF}_4:\text{Yb}^{3+},\text{Er}^{3+}$ NC materials (f).

approximately 200 K becomes smaller than the instrumental step indicating magnetothermal unblocking of the NPs. These observations stay in agreement with the ZFC-FC measurements and indicate that due to the small size of the nanoparticles, their macrospins are thermally unstable at higher temperatures.

The ZFC-FC measurement for the $\text{NaYF}_4:\text{Yb}^{3+},\text{Er}^{3+}$ NPs is shown in Fig. 6b. In both curves, the magnetization decreases with increasing temperature following $1/T$ relation (see inset in Fig. 6b) in the whole measured temperature range. This indicates the purely paramagnetic nature of the material. The magnetization dependencies on the external magnetic field (Fig. 6e) show a gradual reduction of the saturation magnetization with temperature and no coercive field in any case. These results support the ZFC-FC data and are evidence for the paramagnetic behaviors of the material. A similar tendency of the ZFC-FC curves is observed for the $\text{FeS}_2@\text{NaYF}_4:\text{Yb}^{3+},\text{Er}^{3+}$ NC, only observed change is that magnetization reaches 0.04 emu g⁻¹ for NC when for NPs the maximum value of magnetization at 5 K is 0.025 emu g⁻¹. Such a small value of the magnetization compared to the bare FeS_2 is the result of the small contribution of the FeS_2 core mass in the total mass of synthesized NC, *i.e.*, the mass of the shell material was 6.7-fold higher than the core mass.

4. Conclusions

A novel and multifunctional core@shell type $\text{FeS}_2@\text{NaYF}_4:\text{Yb}^{3+},\text{Er}^{3+}$ NC has been synthesized *via* the hydrothermal method, combining the unique properties of the magnetic nano-sized core with UC photoluminescence of the external shell. The structural and morphological properties of the mentioned NC and the corresponding bare NPs were investigated

via XRD, TEM, and Raman spectroscopy. The impact of the Fe^{2+} to S^{2-} ratio (Fe : S) and surfactants used during the synthesis process for the structural properties of the final compounds was analyzed in detail and discussed. The optimized FeS_2 NPs, exhibiting good magnetic properties and weak plasmonic features, were used for the synthesis of luminescent-magnetic $\text{FeS}_2@\text{NaYF}_4:\text{Yb}^{3+},\text{Er}^{3+}$ core@shell NC materials. The UC photoluminescence properties of the bare $\text{NaYF}_4:\text{Yb}^{3+},\text{Er}^{3+}$ NPs and the $\text{FeS}_2@\text{NaYF}_4:\text{Yb}^{3+},\text{Er}^{3+}$ core@shell NC were compared. Both materials exhibit excellent UC luminescence properties. Importantly, the emission color of the NC material can be tuned by the presence of the FeS_2 core, as a result of partial reabsorption of the upconversion emissions by the magnetic phase. Moreover, the luminescence color of both materials, *i.e.*, NPs and NCs can be finely tuned by varying the applied laser power density of the excitation beam, as well as by the temperature change of the environment. Hence, the investigated materials can be used as optical (visual) detectors of the excitation power/energy density of the laser beam, as well as optical temperature sensors (luminescent thermometers). The developed NC material has strong application potential in the fields of biomedicine, optoelectronics, nanotechnology and optical sensors. For example, the magnetic features of the nanomaterial may allow its utilization in magnetic hyperthermia treatment, resulting in local temperature elevation, which can be monitored remotely *via* luminescence thermometry – so by the optically active phase of the developed core@shell NC.

Author contributions

Conceptualization: P. W. and M. R.; methodology: P. W., K. S., and M. P.; validation: K. S. and M. P.; formal analysis: P. W. and



M. P.; investigation: P. W., J. M., and K. S.; resources: M. R. and P. W.; data curation: P. W. and K. S.; writing – original draft preparation: P. W. and M. P., writing – review and editing: P. W. and M. R.; visualization: P. W., K. S., M. P. and J. M.; supervision: M. R. and S. L.; project administration: P. W. and M. R.; and funding acquisition: P. W. and M. R. All authors have read and agreed to the published version of the manuscript.

Data availability

The data supporting this article have been included as part of the ESI.†

Conflicts of interest

There are no conflicts to declare.

Acknowledgements

This work was supported by the Polish National Science Centre grant no. 2018/31/N/ST5/00636 and 2023/50/E/ST5/00021.

References

- 1 X. Hu, M. Wang, F. Miao, J. Ma, H. Shen and N. Jia, Regulation of multifunctional mesoporous core–shell nanoparticles with luminescence and magnetic properties for biomedical applications, *J. Mater. Chem. B*, 2014, **2**(16), 2265–2275, DOI: [10.1039/C3TB21702G](https://doi.org/10.1039/C3TB21702G).
- 2 M. M. Rahman, C. Nguyen, Z. Yan, M. Bolding and O. T. Mefford, Synthesis of iron oxide nanocubes and their incorporation with luminescent lanthanide (Ln = Tb/Eu)-Terephthalate complex in silica nanospheres using a reverse microemulsion method, *J. Solid State Chem.*, 2024, **329**, 124406, DOI: [10.1016/j.jssc.2023.124406](https://doi.org/10.1016/j.jssc.2023.124406).
- 3 H.-T. Wong, H. L. W. Chan and J. H. Hao, Magnetic and luminescent properties of multifunctional GdF₃:Eu³⁺ nanoparticles, *Appl. Phys. Lett.*, 2009, **95**(2), 022512, DOI: [10.1063/1.3177194](https://doi.org/10.1063/1.3177194).
- 4 S. Müssig, J. Reichstein, F. Miller and K. Mandel, Colorful Luminescent Magnetic Supraparticles: Expanding the Applicability, Information Capacity, and Security of Micrometer-Scaled Identification Taggants by Dual-Spectral Encoding, *Small*, 2022, **18**(13), 2107511, DOI: [10.1002/smll.202107511](https://doi.org/10.1002/smll.202107511).
- 5 B. Min and M. Wenzhong, Study on core–shell–shell structured nanoparticles with magnetic and luminescent features: Construction, characterization and oxygen-sensing behavior, *J. Lumin.*, 2013, **141**, 80–86, DOI: [10.1016/j.jlumin.2013.03.028](https://doi.org/10.1016/j.jlumin.2013.03.028).
- 6 M. Schäferling and U. Resch-Genger, Luminescent Nanoparticles for Chemical Sensing and Imaging, *Rev. Fluoresc.*, 2017, 71–109, DOI: [10.1007/978-3-319-48260-6_5](https://doi.org/10.1007/978-3-319-48260-6_5).
- 7 R. Henríquez, *et al.*, Phase-pure iron pyrite (FeS₂) micro- and nano-sized crystals synthesized by simple one-step microwave-assisted hydrothermal method, *Phys. E*, 2019, **118**, 113881, DOI: [10.1016/j.physe.2019.113881](https://doi.org/10.1016/j.physe.2019.113881).
- 8 S. Hunger and L. G. Benning, Greigite: A true intermediate on the polysulfide pathway to pyrite, *Geochem. Trans.*, 2007, **8**, 1–20, DOI: [10.1186/1467-4866-8-1](https://doi.org/10.1186/1467-4866-8-1).
- 9 M. Khabbaz and M. H. Entezari, Simple and versatile one-step synthesis of FeS₂nanoparticles by ultrasonic irradiation, *J. Colloid Interface Sci.*, 2016, **470**, 204–210, DOI: [10.1016/j.jcis.2016.02.055](https://doi.org/10.1016/j.jcis.2016.02.055).
- 10 P. Yu, S. Qu, C. Jia, K. Liu and F. Tan, Modified synthesis of FeS₂ quantum dots for hybrid bulk-heterojunction solar cells, *Mater. Lett.*, 2015, **157**, 235–238, DOI: [10.1016/j.matlet.2015.05.033](https://doi.org/10.1016/j.matlet.2015.05.033).
- 11 G. Kaur, P. D. Sharma, A. Thakur, M. Kumar, R. Bala and A. Kumar, Synthesis of nanostructured marcasite FeS₂ for energy storage applications, *AIP Conf. Proc.*, 2018, **1953**, 2–6, DOI: [10.1063/1.5032421](https://doi.org/10.1063/1.5032421).
- 12 A. M. Huerta-Flores, L. M. Torres-Martínez, E. Moctezuma, A. P. Singh and B. Wickman, Green synthesis of earth-abundant metal sulfides (FeS₂, CuS, and NiS₂) and their use as visible-light active photocatalysts for H₂ generation and dye removal, *J. Mater. Sci. Mater. Electron.*, 2018, **29**(13), 11613–11626, DOI: [10.1007/s10854-018-9259-x](https://doi.org/10.1007/s10854-018-9259-x).
- 13 S. Venkateshalu, P. Goban Kumar, P. Kollu, S. K. Jeong and A. N. Grace, Solvothermal synthesis and electrochemical properties of phase pure pyrite FeS₂ for supercapacitor applications, *Electrochim. Acta*, 2018, **290**, 378–389, DOI: [10.1016/j.electacta.2018.09.027](https://doi.org/10.1016/j.electacta.2018.09.027).
- 14 H. Qin, J. Jia, L. Lin, H. Ni, M. Wang and L. Meng, Pyrite FeS₂ nanostructures: Synthesis, properties and applications, *Mater. Sci. Eng. B*, 2018, **236–237**, 104–124, DOI: [10.1016/j.mseb.2018.11.003](https://doi.org/10.1016/j.mseb.2018.11.003).
- 15 B. Li, L. Huang, M. Zhong, Z. Wei and J. Li, Electrical and magnetic properties of FeS₂ and CuFeS₂ nanoplates, *RSC Adv.*, 2015, **5**(111), 91103–91107, DOI: [10.1039/C5RA16918F](https://doi.org/10.1039/C5RA16918F).
- 16 Y. Chen, Y. Zheng, X. Zhang, Y. Sun and Y. Dong, Solvothermal synthesis of nanocrystalline FeS₂, *Sci. China, Ser. G: Phys., Mech. Astron.*, 2005, **48**(2), 188–200, DOI: [10.1360/04yw0152](https://doi.org/10.1360/04yw0152).
- 17 B. Thomas, K. Ellmer, W. Bohne, J. Röhrich, M. Kunst and H. Tributsch, Photoeffects in cobalt doped pyrite (FeS₂) films, *Solid State Commun.*, 1999, **111**(5), 235–240, DOI: [10.1016/S0038-1098\(99\)00213-6](https://doi.org/10.1016/S0038-1098(99)00213-6).
- 18 A. Yamamoto, M. Nakamura, A. Seki, E. L. Li, A. Hashimoto and S. Nakamura, Pyrite (FeS₂) thin films prepared by spray method using FeSO₄ and (NH₄)₂Sx, *Sol. Energy Mater. Sol. Cells*, 2003, **75**(3–4), 451–456, DOI: [10.1016/S0927-0248\(02\)00205-2](https://doi.org/10.1016/S0927-0248(02)00205-2).
- 19 M. Alam Khan, J. C. Sarker, S. Lee, S. C. Mangham and M. O. Manasreh, Synthesis, characterization and processing of cubic iron pyrite nanocrystals in a photovoltaic cell, *Mater. Chem. Phys.*, 2014, **148**(3), 1022–1028, DOI: [10.1016/j.matchemphys.2014.09.013](https://doi.org/10.1016/j.matchemphys.2014.09.013).
- 20 X. H. Tian and J. M. Zhang, The electronic, magnetic and optical properties of Co doped marcasite FeS₂, *J. Phys.*



Chem. Solids, 2018, **121**, 285–291, DOI: [10.1016/j.jpcs.2018.05.039](https://doi.org/10.1016/j.jpcs.2018.05.039).

21 X. Zhang, *et al.*, Tuning localized surface plasmon resonances of FeS₂ nanocrystals via shape and surface functional groups for enhanced photoconductivity, *J. Mater. Sci. Mater. Electron.*, 2017, **28**(17), 12717–12725, DOI: [10.1007/s10854-017-7097-x](https://doi.org/10.1007/s10854-017-7097-x).

22 N. Jurga, D. Przybylska, P. Kamiński, A. Tymiński, B. F. Grześkowiak and T. Grzyb, Influence of the synthesis route on the spectroscopic, cytotoxic, and temperature-sensing properties of oleate-capped and ligand-free core/shell nanoparticles, *J. Colloid Interface Sci.*, 2022, **606**, 1421–1434, DOI: [10.1016/j.jcis.2021.08.093](https://doi.org/10.1016/j.jcis.2021.08.093).

23 D. T. Klier and M. U. Kumke, Analysing the effect of the crystal structure on upconversion luminescence in Yb³⁺,Er³⁺-co-doped NaYF₄ nanomaterials, *J. Mater. Chem. C*, 2015, **3**(42), 11228–11238, DOI: [10.1039/c5tc02218e](https://doi.org/10.1039/c5tc02218e).

24 C. Renero-Lecuna, *et al.*, Origin of the high upconversion green luminescence efficiency in β -NaYF₄:2%Er³⁺, 20%Yb³⁺, *Chem. Mater.*, 2011, **23**(15), 3442–3448, DOI: [10.1021/cm2004227](https://doi.org/10.1021/cm2004227).

25 S. Saha, R. G. S. Pala and S. Sivakumar, Catalyzing Cubic-to-Hexagonal Phase Transition in NaYF₄ *via* Ligand Enhanced Surface Ordering, *Cryst. Growth Des.*, 2018, **18**(9), 5080–5088, DOI: [10.1021/acs.cgd.8b00535](https://doi.org/10.1021/acs.cgd.8b00535).

26 D. Chávez-García, K. Juárez-Moreno, C. H. Campos, J. B. Alderete and G. A. Hirata, Upconversion rare earth nanoparticles functionalized with folic acid for bioimaging of MCF-7 breast cancer cells, *J. Mater. Res.*, 2018, **33**(2), 191–200, DOI: [10.1557/jmr.2017.463](https://doi.org/10.1557/jmr.2017.463).

27 D. Chávez-García, K. Juárez-Moreno, C. H. Campos, E. M. Tejeda, J. B. Alderete and G. A. Hirata, Cytotoxicity, genotoxicity and uptake detection of folic acid-functionalized green upconversion nanoparticles Y₂O₃/Er³⁺, Yb³⁺ as biolabels for cancer cells, *J. Mater. Sci.*, 2018, **53**(9), 6665–6680, DOI: [10.1007/s10853-017-1946-0](https://doi.org/10.1007/s10853-017-1946-0).

28 L. F. Dos Santos, *et al.*, In vitro assays and nanothermometry studies of infrared-to-visible upconversion of nanocrystalline Er³⁺,Yb³⁺ co-doped Y₂O₃ nanoparticles for theranostic applications, *Phys. Rev. B: Condens. Matter Mater. Phys.*, 2021, **624**, 413447, DOI: [10.1016/j.physb.2021.413447](https://doi.org/10.1016/j.physb.2021.413447).

29 M. R. Hamblin, Upconversion in photodynamic therapy: plumbing the depths, *Dalton Trans.*, 2018, **47**(26), 8571–8580, DOI: [10.1039/C8DT00087E](https://doi.org/10.1039/C8DT00087E).

30 Q. Zhang, S. Yue, H. Sun, X. Wang, X. Hao and S. An, Nondestructive up-conversion readout in Er/Yb co-doped Na_{0.5}Bi_{2.5}Nb₂O₉ -based optical storage materials for optical data storage device applications, *J. Mater. Chem. C*, 2017, **5**(15), 3838–3847, DOI: [10.1039/C7TC00582B](https://doi.org/10.1039/C7TC00582B).

31 A. Szczeszak, *et al.*, Upconversion luminescence in cellulose composites (fibres and paper) modified with lanthanide-doped SrF₂ nanoparticles, *J. Mater. Chem. C*, 2020, **8**(34), 11922–11928, DOI: [10.1039/D0TC02050H](https://doi.org/10.1039/D0TC02050H).

32 M. Runowski, *et al.*, Lifetime nanomanometry-high-pressure luminescence of up-converting lanthanide nanocrystals-SrF₂:Yb³⁺,Er³⁺, *Nanoscale*, 2017, **9**(41), 16030–16037, DOI: [10.1039/c7nr04353h](https://doi.org/10.1039/c7nr04353h).

33 N. Stopikowska, M. Runowski, M. Skwierczyńska and S. Lis, Improving performance of luminescent nanothermometers based on non-thermally and thermally coupled levels of lanthanides by modulating laser power, *Nanoscale*, 2021, **13**(33), 14139–14146, DOI: [10.1039/d1nr01395e](https://doi.org/10.1039/d1nr01395e).

34 Q. Bao, *et al.*, Graphene-Polymer Nanofiber Membrane for Ultrafast Photonics, *Adv. Funct. Mater.*, 2010, **20**(5), 782–791, DOI: [10.1002/adfm.200901658](https://doi.org/10.1002/adfm.200901658).

35 M. Skwierczyńska, P. Woźny, M. Runowski, M. Perzanowski, P. Kulpiński and S. Lis, Bifunctional magnetic-upconverting luminescent cellulose fibers for anticounterfeiting purposes, *J. Alloys Compd.*, 2020, **829**, 154456, DOI: [10.1016/j.jallcom.2020.154456](https://doi.org/10.1016/j.jallcom.2020.154456).

36 Y. Tang, *et al.*, The role of surface chemistry in determining *invivo* biodistribution and toxicity of CdSe/ZnS core-shell quantum dots, *Biomaterials*, 2013, **34**(34), 8741–8755, DOI: [10.1016/j.biomaterials.2013.07.087](https://doi.org/10.1016/j.biomaterials.2013.07.087).

37 M. Runowski and S. Lis, Synthesis, surface modification/decoration of luminescent-magnetic core/shell nanomaterials, based on the lanthanide doped fluorides (Fe₃O₄/SiO₂/NH₂/PAA/LnF₃), *J. Lumin.*, 2016, **170**, 484–490, DOI: [10.1016/j.jlumin.2015.05.037](https://doi.org/10.1016/j.jlumin.2015.05.037).

38 C. F. Holder and R. E. Schaak, “Tutorial on Powder X-ray Diffraction for Characterizing Nanoscale Materials,” *ACS Nano*, 2019, **13**(7), 7359–7365, DOI: [10.1021/acsnano.9b05157](https://doi.org/10.1021/acsnano.9b05157).

39 M. Alam Khan, J. C. Sarker, S. Lee, S. C. Mangham and M. O. Manasreh, Synthesis, characterization and processing of cubic iron pyrite nanocrystals in a photovoltaic cell, *Mater. Chem. Phys.*, 2014, **148**(3), 1022–1028, DOI: [10.1016/j.matchemphys.2014.09.013](https://doi.org/10.1016/j.matchemphys.2014.09.013).

40 D. Yang, *et al.*, Controllable Phase Transformation and Mid-infrared Emission from Er³⁺-Doped Hexagonal-/Cubic-NaYF₄ Nanocrystals, *Sci. Rep.*, 2016, **6**(1), 29871, DOI: [10.1038/srep29871](https://doi.org/10.1038/srep29871).

41 H. Assaaoudi, G.-B. Shan, N. Dyck and G. P. Demopoulos, Annealing-induced ultra-efficient NIR-to-VIS upconversion of nano-/micro-scale α and β NaYF₄:Er³⁺,Yb³⁺ crystals, *CrysEngComm*, 2013, **15**(23), 4739, DOI: [10.1039/c3ce40362a](https://doi.org/10.1039/c3ce40362a).

42 C. Dubey, A. Yadav, D. Baloni, S. Kachhap, S. K. Singh and A. K. Singh, Impact of crystal structure on optical properties and temperature sensing behavior of NaYF₄:Yb³⁺/Er³⁺ nanoparticles, *RSC Adv.*, 2023, **13**(30), 20975–20983, DOI: [10.1039/D3RA03148A](https://doi.org/10.1039/D3RA03148A).

43 M. Runowski, N. Stopikowska and S. Lis, UV-Vis-NIR absorption spectra of lanthanide oxides and fluorides, *Dalton Trans.*, 2020, **49**(7), 2129–2137, DOI: [10.1039/C9DT04921E](https://doi.org/10.1039/C9DT04921E).

44 N. Jurga, D. Przybylska, P. Kamiński, A. Tymiński, B. F. Grześkowiak and T. Grzyb, Influence of the synthesis route on the spectroscopic, cytotoxic, and temperature-sensing properties of oleate-capped and ligand-free core/shell nanoparticles, *J. Colloid Interface Sci.*, 2022, **606**, 1421–1434, DOI: [10.1016/j.jcis.2021.08.093](https://doi.org/10.1016/j.jcis.2021.08.093).

45 T. Grzyb, S. Balabhadra, D. Przybylska and M. Węclawiak, “Upconversion luminescence in BaYF₅, BaGdF₅ and BaLuF₅ nanocrystals doped with Yb³⁺/Ho³⁺, Yb³⁺/Er³⁺ or



Yb³⁺/Tm³⁺ ions," *J. Alloys Compd.*, 2015, **649**, 606–616, DOI: [10.1016/j.jallcom.2015.07.151](https://doi.org/10.1016/j.jallcom.2015.07.151).

46 R. B. Anderson, S. J. Smith, P. S. May and M. T. Berry, Revisiting the NIR-to-Visible Upconversion Mechanism in β -NaYF₄:Yb³⁺,Er³⁺, *J. Phys. Chem. Lett.*, 2014, **5**(1), 36–42, DOI: [10.1021/jz402366r](https://doi.org/10.1021/jz402366r).

47 M. T. Berry and P. S. May, Disputed Mechanism for NIR-to-Red Upconversion Luminescence in NaYF₄:Yb³⁺,Er³⁺, *J. Phys. Chem. A*, 2015, **119**(38), 9805–9811, DOI: [10.1021/acs.jpca.5b08324](https://doi.org/10.1021/acs.jpca.5b08324).

48 C. Hernández-Álvarez, *et al.*, Multifunctional optical sensing platform of temperature, pressure (vacuum) and laser power density: NaYF₄:Gd³⁺, Yb³⁺, Er³⁺ nanomaterial as luminescent thermometer, manometer and power meter, *J. Mater. Chem. C*, 2023, **11**(30), 10221–10229, DOI: [10.1039/D3TC01712E](https://doi.org/10.1039/D3TC01712E).

49 M. Runowski, P. Woźny and I. R. Martín, Optical pressure sensing in vacuum and high-pressure ranges using lanthanide-based luminescent thermometer-manometer, *J. Mater. Chem. C*, 2021, **9**(13), 4643–4651, DOI: [10.1039/d1tc00709b](https://doi.org/10.1039/d1tc00709b).

